Delft University of Technology

Study on the Mg-Li-Zn ternary alloy system with improved mechanical properties, good degradation performance and different responses to cells

Liu, Yang; Wu, Yuanhao; Bian, Dong; Gao, Shuang; Leeflang, Sander; Guo, Hui; Zheng, Yufeng; Zhou, Jie

Important note
To cite this publication, please use the final published version (if applicable).
Please check the document version above.

Study on the Mg-Li-Zn ternary alloy system with improved mechanical properties, good degradation performance and different responses to cells

Yang Liu[a], Yuanhao Wu[b], Dong Bian[a], Shuang Gao[b], Sander Leeflang[c], Hui Guo[a], Yufeng Zheng[a,b,*] Jie Zhou[c,**]

[a] *Department of Materials Science and Engineering, College of Engineering, Peking University, Beijing 100871, China*

[b] *Center for Biomedical Materials and Tissue Engineering, Academy for Advanced Interdisciplinary Studies, Peking University, Beijing 100871, China*

[c] *Department of Biomechanical Engineering, Delft University of Technology, Mekelweg 2, 2628 CD Delft, The Netherlands*

*Corresponding Author: Prof. Yufeng Zheng, Department of Materials Science and Engineering, College of Engineering, Peking University, Beijing 100871, China. Tel&Fax: 0086-10-6276 7411. E-mail: yfzheng@pku.edu.cn

**Co-corresponding Author: Prof. Jie Zhou, Department of Biomechanical Engineering, Delft University of Technology, Mekelweg 2, 2628 CD Delft, The Netherlands. Tel: +31(0) 15 27 85357. E-mail: j.zhou@tudelft.nl

Abstract

Novel Mg-(3.5, 6.5, wt.%)Li-(0.5, 2, 4, wt.%)Zn ternary alloys were developed as a new kind of biodegradable metallic materials potentially for stent applications. Their mechanical properties, degradation behavior, cytocompatibility and hemocompatibility were studied. These potential biomaterials showed higher ultimate strengths than those of previously reported binary Mg-Li alloys and ternary Mg-Li-X (X=Al, Y, Ce, Sc, Mn and Ag) alloys. Among the alloys studied, the Mg-3.5Li-2Zn and Mg-6.5Li-2Zn alloys exhibited comparable corrosion resistance in Hank's solution to pure magnesium and better corrosion resistance in a cell culture medium than pure magnesium. Corrosion products observed on the corroded surface, were composed of $Mg(OH)_2$, $MgCO_3$ and Ca-free Mg/P inorganics and Ca/P inorganics. In vitro cytotoxicity assay revealed different behaviors of Human Umbilical Vein Endothelial Cells (HUVECs) and Human Aorta Vascular Smooth Muscle Cells (VSMCs) to material extracts. HUVECs showed increased nitric oxide (NO) release and tolerable toxicity, whereas VSMCs exhibited steadily decreased viability with time. Platelet adhesion, hemolysis and coagulation tests of these Mg-Li-Zn alloys showed different degrees of activation behavior, in which the hemolysis of the Mg-3.5Li-2Zn alloy was lower than 5%. These results indicated the potential of Mg-Li-Zn alloys as good candidate materials for cardiovascular stent application.

1. Introduction

From the viewpoint of materials science and engineering, an addition of lithium (density: 0.534 g·cm^3) to magnesium can make a light alloy with a high specific strength. With increasing content of lithium in the magnesium-lithium system, the constitutional phase changes from the single α-phase (0-5.7 wt.% Li) having a hexagonal closed-packed (hcp) crystal structure to the α+β dual phases (5.7-10.3 wt.% Li) and then to the single β-phase (>10.3 wt.% Li) having a body-centered cubic (bcc) crystal structure. It is well known that a material with a bcc structure is in general more ductile than a material with a hcp structure due to the activation of more slip systems in the former and a crystal structure transition from hcp to bcc leads to an enhanced room temperature ductility of a Mg-Li-based alloy up to 80% [1, 2], which is superior to the ductility of any other Mg-based alloys and significant for applications where ductility is of prime importance, for example, for vascular stents. However, the corrosion performance of Mg-Li-based alloys is still a highly controversial issue in the papers published. A reduction in corrosion resistance is basically related to the high chemical reactivity of lithium, which limits the applications of Mg-Li-based alloys [3, 4]. However, the high corrosion susceptibility of Mg-Li-based alloys can be suppressed to a certain extent. A special thermal and mechanical treatment has recently been successfully applied to a Mg-Li-Al-Zr-Y alloy with a Li content of 10.95 wt.% to form complex surface layers, leading to corrosion resistance better than pure Mg or other hcp-structured Mg alloys [5].

In the biomedical field, lithium has been adopted in the treatment of bipolar disorder [6] and lithium salts are believed to be helpful in diagnosing schizoaffective disorder, cyclic major depression [7] and cluster headaches [8]. In addition, the role of lithium in cardiovascular treatment has in recent years been recognized. For example, Li has been found to induce the

release of nitric oxide (NO) in brain vascular cells [9, 10]. Mg-Li-Ca and Mg-Li-Al-RE alloys have been reported to be promising biodegradable alloys, especially for stent application. The dual phases in the Mg-9.29Li-0.88Ca alloy have been reported to be associated with a multi-layer structured surface film, leading to a corrosion process in Hank's solution different from that of common Mg alloys with one phase being attacked and another being protected [11]. Mg-Li-based alloys with the addition of rare earth elements, intended for stent application, have been found to perform well in corrosion resistance during static immersion tests and possess good cytocompatibility [12].

Zinc is well known for being an essential element in human nutrition. It is associated with numerous biological functions such as nucleic acid metabolism, signal transduction, gene expression, apoptosis regulation and endocrine regulation [13]. Furthermore, zinc has been found to possess physiological corrosion resistance ideal for biodegradable stents [14]. Zn-Li binary alloys have shown not only good corrosion resistance but also good mechanical properties, both of which are needed for stent application [15]. From the perspective of material science, an addition of zinc to magnesium may lead to improved mechanical properties and corrosion resistance as long as its concentration does not go beyond a certain limit [16, 17].

In this study, a series of Mg-Li-Zn alloys were designed, and their microstructure, surface characteristics, mechanical properties, corrosion performance, oxidation behavior, in vitro cytocompatibility as well as in vitro hemocompatibility were comprehensively investigated. The study was aim at exploring the feasibility to develop a Mg-Li-Zn alloy system specifically for stent application where biodegradability, biocompatibility, strength and ductility are all required.

2. Materials and Methods

2.1 Material preparation

Mg-(3.5, 6.5, wt.%)Li-(0.5, 2, 4, wt.%)Zn alloys were prepared in Zhengzhou Light Metals Research Institute, China Aluminum Corporation. The analyzed compositions are shown in Table 1. High purity Mg (99.98%) was used as a control group. Ingots of the alloys and pure Mg were extruded at 280 °C and at a reduction ratio of 16 into bars. Disk-shape samples for microstructure, surface chemistry, corrosion tests, in vitro cell viability and hemocompatibility (with sizes of $\Phi 10 \times 2$ mm^3) were cut from the extruded bars and mechanically polished, followed by cleaning and drying in air.

2.2 Microstructure and surface characterization

An optical microscope (BX51M, Olympus) was used to observe the microstructures of the alloys prepared. Polished samples were etched in a 2% nitric acid alcohol solution and rinsed in distilled water. An X-ray diffractometer (XRD DMAX 2400, Rigaku) with Cu Kα radiation and at a scan rate of 4 °/min was used to detect the phase compositions of the samples. The surface chemistry was determined with an X-ray photoelectron spectroscope (XPS Axis Ultra, Kratos Analytical) with Al Kα radiation. High resolution narrow scanning was conducted to determine the binding state of Mg 2p, Li 1S, Zn 2p, O 1s and C 1s. Surface morphologies were observed with an SEM coupled with EDS (S-4800 Emission Scanning Electron Microscopy, Hitachi).

2.3 Mechanical tests

Tensile specimens were cut from the extruded bars and machined according to ASTM-E8-04a to have a gauge length of 25 mm. Tensile tests were carried out at a crosshead speed of 1 mm/min and at room temperature using an Instron 5969 machine. At least, three specimens for each material were tested.

2.4 Electrochemical evaluation

Electrochemical evaluation was conducted using a three-electrode cell with a platinum plate as the counter-electrode and a saturated calomel electrode (SCE) as the reference electrode. The electrochemical tests were carried out in Hank's solution (NaCl 8.00 $g \cdot L^{-1}$, KCl 0.40 $g \cdot L^{-1}$, $CaCl_2$ 20.14 $g \cdot L^{-1}$, $NaHCO_3$ 0.35 $g \cdot L^{-1}$, glucose 1.00 $g \cdot L^{-1}$, $MgCl_2 \cdot 6H_2O$ 0.10 $g \cdot L^{-1}$, $MgSO_4 \cdot 7H_2O$ 0.06 $g \cdot L^{-1}$, $Na_2HPO_4 \cdot 12H_2O$ 0.06 $g \cdot L^{-1}$ and KH_2PO_4 0.06 $g \cdot L^{-1}$, pH=7.4) at room temperature using an electrochemical workstation (Autolab, Metrohm). The surface of a round specimen with a diameter of 5 mm was exposed to Hank's solution. Each specimen first underwent open-circuit potential (OCP) for 4800 s. Afterwards, potentiodynamic polarization was performed at a scanning rate of 1 mV s^{-1}. Corrosion parameters including open-circuit potential (OCP), corrosion potential (E_{corr}) and corrosion current density (i_{corr}) were estimated from the polarization curves by means of Tafel analysis based on the polarization plots. Since the determination of Tafel slope might cause large variations [18], the Tafel slopes were carefully determined in the potential range of 130 to 300 mV away from E_{corr} both on the cathodic curve and the anodic curve. At least three duplicates were tested for each alloy.

2.5 In vitro immersion and hydrogen evolution

Immersion tests with 3 duplicates were performed with a ratio of solution volume to sample surface area (V/S) at 20 $ml \cdot cm^{-2}$, according to ASTM G31-72 in Hank's solution at 37°C. Hydrogen evolution tests with the same V/S ratio at 37°C were conducted using a setup similar to the schematic illustration presented elsewhere [19]. The pH value and the volume of hydrogen evolved were recorded at each time point. At 3 and 20 d, samples were taken out of the solution,

immersed in deionized water and dried in air. Surface and interface morphologies were observed with SEM and the ion concentrations of the solution after 20 days of the immersion tests were determined using an Inductively Coupled Plasma-Atomic Emission Spectrometer (ICP-AES, PROFILE SPEC, Leeman). In addition, surface morphologies as well as cross section morphologies before and after natural oxidization were investigated with SEM coupled with EDS, operating in the SEM mode and the backscattering electron (BSE) mode. The functional groups in the corrosion products were detected by means of microscopic Fourier Transform Infrared analysis (Spotlight 200 Micro-FTIR, PerkinElmer). The spectra were recorded from 4000 to 650 cm^{-1}. Small angle X-ray diffraction was conducted by using X'Pert PRO MDP (Panalytical) with Cu Kα radiation at 0.5° over a scan range from 10 to 90°.

2.6 Cell viability assay, cell morphology and NO release

Cell viability and proliferation evaluation was conducted according to ASTM 10993-5: 2009. Human Umbilical Vein Endothelial Cells (HUVECs) and Human Aorta Vascular Smooth Muscle Cells (HA-VSMCs) were utilized. Cells were obtained from American Type Culture Collection (ATCC) and maintained in our laboratory. Cells were separately cultured in Dulbecco's Modified Eagle's Medium (DMEM) supplemented with 10% fetal bovine serum (FBS), 100 $U \cdot ml^{-1}$ penicillinand and 100 $g \cdot ml^{-1}$ streptomycin in a humidified atmosphere with 5% CO_2 at 37 °C. Cell viability, morphology and NO release were all determined with the indirect method. Polished samples were washed, dried in air and sterilized. Extracts were generated by incubating the samples in DMEM supplemented with 10% FBS for 24 h at an extraction ratio of 1 $cm^2 \cdot ml^{-1}$. Ion concentrations in the gathered extracts were determined using an Inductively Coupled Plasma Optical Emission Spectroscope (ICP-OES, iCAP6300, Thermo). The extract of

the as-extruded pure Mg (99.98% purity) was utilized as the material control, the cell culture medium as the negative control and the culture medium added with 10% dimethylsulfoxide (DMSO) as the positive control.

As to the in vitro viability assay, cells were seeded in 96-well plates at a density of 5×10^3 cells per 100 μL medium and incubated for 24 h to allow attachment. Then, the cell culture medium was replaced by the extracts. At 1, 3 and 5 d, the extracts were replaced by the cell culture medium and then 10 μL CCK-8 was added to each well and restored in an incubator for 1 h. The spectrophotometric absorbance of each well was measured with a microplate reader (Bio-RAD 680) at a single wavelength of 450 nm. At least 6 duplicates were adopted for the in vitro viability assay.

The influence of extracted ions on cell morphology was evaluated using a Laser Scanning Confocal Microscope (A1R-si, Nikon) and a glass slide with a thickness of 0.17 mm. 0.5 ml of cell suspensions in 24-well plate were placed on a glass slide at a density of 5×10^4 cells per milliliter and incubated for 24 h to allow attachment to the glass slide. Then, the media were replaced by extracts and incubated for 24 h. After that, the HUVEC culture extracts were obtained for NO release tests and both HUVECs and VSMCs were thoroughly washed by PBS and fixed by 4% paraformaldehyde for 10 min at room temperature. 0.1% Triton was then added and reacted for 7 min. 5 μg·ml^{-1} FITC-phalloidin dye for microfilament was added to the PBS-rinsed well and incubated for 30 min at room temperature. 10 μg·ml^{-1} DAPI dye for nuclei was then added and incubated for 10 min at 37 °C. The cell morphology was visualized with a confocal microscope at excitation wavelengths of 405 and 488 nm. Three duplicates were utilized for observation. The NO release tests of the 24 h culture extract of HUVECs were

conducted using a NO detection kit (Nanjing Jiancheng Bioengineering Institute), following the protocol. Three duplicates were used for the NO release tests.

2.7 Hemolysis and platelet adhesion

Human blood from a healthy volunteer was anticoagulated with 3.8 wt.% sodium citrate at a ratio of 9:1 and diluted with normal saline at a volume ratio of 4:5. Samples were then incubated in 10 mL normal saline at 37 °C for 30 min. Then 0.2 mL diluted blood was further incubated for another 60 min. Normal saline and deionized water were set as the negative group and positive group, respectively. All tubes were centrifuged at 3000 rpm for 5 min and the supernatant was carefully transferred to 96-well plate. Absorbance was read by a microplate reader (Bio-RAD 680) at a single wavelength of 545 nm. The hemolysis was calculated according to the following equation:

$$\text{Hemolysis rate} = \frac{\text{OD (testing group)} - \text{OD (negative group)}}{\text{OD (positive group)} - \text{OD (negative group)}} \times 100\%$$

Adhesion and activation performances of the platelets were determined through the platelet adhesion test. Platelet-Rich Plasma (PRP) was prepared by centrifuging anticoagulated whole blood at 1000 rpm for 10 min. 0.2 mL PRP was dropped on the surface of sample. Afterwards, PBS was used to rinse surface, followed by platelet fixation for 2 h in a 2.5 % glutaraldehyde-PBS solution, dehydrating in gradient ethanol/distilled water solutions (50, 60, 70, 80, 90 and 100%) for 10 min each and drying in air. The morphologies of adhered platelets were observed by using SEM (S4800, Hitachi).

2.8 Coagulation four

The activated partial thromboplastin time (APTT), prothrombin time (PT), fibrinogen (FIB-C) and thrombin time (TT) were measured in a coagulometer (ACL TOP, Instrumentation Laboratory Co). Fresh human platelet poor plasma (PPP) was prepared by centrifugation at 3000 rpm for 15 min. Afterwards, PPP was transferred to an anticoagulative tube without sodium citrate. The four biochemical indexes were measured at Peking University People's Hospital.

2.9 Statistical analysis

Statistical analysis was performed with SPSS 18.0 for Windows Software (SPSS Inc., Chicago, USA). One-way analysis of variance (ANOVA) followed by Tukey post hoc tests was used to statistically analyze all the data. A *p*-value <0.05 was considered statistically significant.

3. Results

3.1 Microstructures

The microstructures of the materials are shown in Figure 1a. With the Li content being 3.5 wt.%, the alloys had a single light phase (α phase) and dark particles which increased with increasing Zn content. The dark Zn-containing particles changed from small particles and large aggregates in Mg-3.5Li-0.5Zn, to finely distributed particles in Mg-3.5Li-2Zn to evenly distributed particles with a stream pattern in Mg-3.5Li-4Zn. As the content of Li increased to 6.5 wt.%, both the light α-phase and dark β-phase were observed (Mg-6.5Li-xZn). XRD results (Figure 1b) confirmed the single α phase in the Mg-3.5Li-xZn alloys and the dual α+β phases in the Mg-6.5Li-xZn alloys. However, no Zn-containing phase was detected in XRD even when the addition of Zn to Mg was 4 wt.%. It may be because the fact that Zn has significant large solid solubility in both Mg and Li, leaving Zn-containing particles not detected by XRD. Nevertheless, SEM coupled

EDS confirmed the presence of Zn-containing compounds along the edge of the stream pattern in the form of aggregated particles (Figure 1c).

3.2 Surface characteristics

The surface chemistry of the alloys was determined using XPS. The XPS files of Mg-3.5Li-2Zn and Mg-6.5Li-2Zn are shown in Figure 2, while the XPS spectra of the other Mg-Li-Zn alloys are shown in Figure S1. In general, C, O, Li and Mg were detected, with concentration and chemical valence variations depending on alloy composition. The relative broad peak of O 1s indicated a mixture of O at different chemical states. Interestingly, from all of the XPS spectra, no sign of zinc was found on the surface, indicating a very limited amount of Zn on the naturally formed surface film. In the Mg-3.5Li-based alloys, more Mg was detected on the surface (Figure 2a, Figure S1d and Figure S1h), whilst in the Mg-6.5Li-based alloys a much stronger peak of Li 1s was detected (Figure 2b, Figure S1l and Figure S1p). Although no Zn was detected on the surface, the surface Mg/Li ratio reached its highest with Zn at 2.0 wt.% in both the Mg-6.5Li-xZn and Mg-3.5Li-xZn alloys. To reveal chemical state differences, the detected elements were all further investigated with high resolution scan. In the Mg-3.5Li-2Zn alloy, one Li 1s peak assigned to 55.1 eV, accompanied by C 1s at 290.1 eV and O 1s at 531.7 eV, was detected, suggesting the presence of Li_2CO_3 [5, 20]. In addition, the broad peak range of O 1s suggested different chemical states of O present on the surface. The results also confirmed the predominant presence of Mg-based compounds, including $MgO/Mg(OH)_2$ and/or $MgCO_3$ [21, 22]. As expected, with Li content increasing, the predominant presence of Mg and Li switched, due to the change in phase composition. Li_2O (Li 1s 54.0 eV) instead of $MgCO_3$ appeared on the surface of the Mg-6.5Li-2Zn alloy, in addition to Li_2CO_3 and MgO [23]. The other two Mg-6.5Li-xZn alloys showed the similar phase compositions on the surface. It should be mentioned

that although no sign of LiOH was found, it was considered to be present due to the absorption of H_2O to Li_2O. In general, our XPS results confirmed the surface chemistry of the alloys with Li_2CO_3 and Mg-based compounds as the main phases. Furthermore, Zn seemed to act as a mediator to influence the surface Mg/Li ratio but did not interfere the surface phase composition.

3.3 Mechanical properties

The tensile properties of the Mg-Li-Zn alloys are shown in Figure 3. The combined addition of Li and Zn greatly improved the yield strength (YS), ultimate tensile strength (UTS) and elongation of pure magnesium. The YS and elongation values of the Mg-Li-Zn alloys were at least two times as high as those of the control pure Mg. More specifically, the UTS values of Mg-3.5Li-2Zn and Mg-3.5Li-4Zn exceeded 245 MPa (i.e., 246.3±1.5 and 250.4±12.7 MPa, respectively), up 48% from the value of pure Mg. With respect to elongation, both the Mg-6.5Li-2Zn and Mg-6.5Li-4Zn alloys reached high values, i.e., 29.4±1.8% and 34.9±0.6%, respectively, representing the increases of 2 and 3 times from the value of pure Mg (11.6±0.7%). The increases in mechanical properties could be attributed to the microstructural changes brought about by the alloying elements and by the processes that the alloys went through. In the case of the Mg-3.5Li-xZn alloys, the matrix is still the hcp-structured α-Mg phase with solute Li and Zn-containing compounds. Thus, the improvements in tensile strength and elongation must be due to the hot extrusion process which led to grain refinement, in addition to solution strengthening and dispersion strengthening. The Mg-6.5Li-xZn alloys contain both the hcp-structured α-phase and bcc-structured β-phase. In the bcc-structured β-phase more slip systems are activated at room temperature, as compared with the hcp-structured α-phase, which made these alloys easy to deform and attain exceptionally large elongation values. The gains of the alloys with the duplex

structure in ductility are accompanied by the losses in YS and UTS, but the overall levels of YS and UST are about 3 times as high as those of common biodegradable polymers [24].

3.4 Electrochemical evaluations

Table 2 summarizes the electrochemical parameters obtained from the electrochemical tests in Hank's solution. Since Li and Zn respectively have more negative (Li: -3.0401 V) and nobler (Zn: -0.7618V) standard hydrogen electrode potentials than Mg (-2.372 V) [25], the combined addition of the two elements resulted in OCP and corrosion potential values quite similar to those of the control pure Mg. The addition of Zn exerted a variable influence on the corrosion behavior of the alloys. The Mg-3.5Li-2Zn alloy showed the best corrosion resistance in the Mg-3.5Li-xZn alloy system, whereas the Mg-6.5Li-2Zn alloy exhibited corrosion resistance inferior to the Mg-6.5Li-0.5Zn alloy, implying the joint influences of Li and Zn. With reference to the microstructure shown in Figure 1, the single α-phase together with finely distributed Zn-containing particles may account for the best corrosion resistance of the Mg-3.5Li-2Zn alloy determined from the electrochemical tests.

The potentiodynamic polarization curves of the Mg-Li-Zn alloys with pure Mg as the control group are shown in Figure 4a. In addition to the shifts of corrosion potential, the Mg-Li-Zn alloys exhibited sharper cathodic reaction curves. From the results of potentiodynamic polarization, it was clear that, among all the Mg-Li-Zn alloys, the Mg-3.5Li-2Zn alloy possessed the lowest corrosion current density. However, the corrosion resistance inferior to that of pure Mg in the electrochemical test showed that the presence of a Li_2CO_3–containing film on the surface could not provide effective protection from the variable potential applied. The other compounds in the surface film originating from the matrix must have weakened the protecting effect of the surface film.

3.5 Immersion tests and hydrogen evolution

The results obtained from the in vitro immersion tests with respect to hydrogen evolution, pH change and ion concentrations are shown in Figure 4b-d. It is obvious that when 4.0 wt.%Zn was added to magnesium, the quantities of evolved hydrogen were much higher than those of the other Mg-Li-Zn alloys with lower Zn contents. The Mg-3.5Li-4Zn alloy showed a high reactivity in Hank's solution and produced over 8 ml·cm^{-2} hydrogen after 240 h immersion. Being in agreement with the results from the electrochemical tests, the corrosion resistance of the alloys did not show a monotonic variation when the Zn content when the Li content was kept unchanged. The alloys containing 0.5 wt.%Zn exhibited weaker corrosion resistance, relative to their counterparts containing 2 wt.% Zn. The total hydrogen evolved from Mg-3.5Li-2Zn and Mg-6.5Li-2Zn alloy samples over a period of 240 h were 0.1088±0.0094 ml·cm^{-2} and 0.3482±0.0094 ml·cm^{-2}, respectively, both of which were lower than the hydrogen produced from pure Mg sample (0.4081±0.0163 ml·cm^{-2}) ($p<0.05$).

The pH values of Hank's solution with Mg-3.5Li-2Zn and Mg-6.5Li-2Zn alloy samples were quite comparable and the trend with immersion time was similar to that of pure Mg ($p>0.05$). The ion concentrations after 20 d immersion in Hank's solution were quite consistent with the results in hydrogen evolution. All the Mg^{2+} concentrations in Hank's solution incubating pure Mg, Mg-3.5Li-2Zn and Mg-6.5Li-2Zn alloy samples were in the range from 80 μg·mL^{-1} to 90 μg·mL^{-1}. The Mg-3.5Li-4Zn alloy released the largest amount of Mg^{2+}, which was 673.36 μg·mL^{-1} at day 20. It was only the Mg-3.5Li-4Zn alloy that released more Zn^{2+} than Li$^+$. The Mg-6.5Li-4Zn alloy released more Li$^+$ than Zn^{2+}, the Zn^{2+} concentration (3.66 μg·mL^{-1}) was much higher that Zn^{2+} concentrations from the other Mg-Li-Zn alloys (all being around 1 μg·mL^{-1}, with 0.53 μg·mL^{-1} being the lowest from the Mg-6.5Li-2Zn alloy. The Li$^+$ concentrations from

most of the Mg-Li-Zn alloys were in the range from 10 $\mu g \cdot mL^{-1}$ to 20 $\mu g \cdot mL^{-1}$, with the lowest at 5.69 $\mu g \cdot mL^{-1}$ from the Mg-3.5Li-2Zn alloy. Comparison between the Mg-3.5Li-2Zn alloy and the Mg-6.5Li-2Zn alloy revealed a reverse relationship in the concentrations of Li^+ and Zn^{2+}; the Zn^{2+} concentration from the Mg-3.5Li-2Zn alloy was double the Zn^{2+} concentration from the Mg-6.5Li-2Zn alloy (1.01 $\mu g \cdot mL^{-1}$ versus 0.53 $\mu g \cdot mL^{-1}$) but the Li^+ concentration from the former was only half the Li^+ concentration from the latter (5.69 $\mu g \cdot mL^{-1}$ versus 12.09 $\mu g \cdot mL^{-1}$). The general surface morphologies of samples immersed in Hank's solution for 20 d are shown in Figure S2, with a detailed description given in the supplemental materials. Figure 5 shows the surface morphologies and elements detected on sample surface, as well as the morphologies of corrosion products observed on the cross section. The Mg-3.5Li-2Zn alloy showed a surface with limited amounts of corrosion products at 3 and 20 d. Obviously, the deposition of Ca and P from Hank's solution on sample surface increased over time, which was also observed on the surface of pure Mg.

On the surfaces of Mg-3.5Li-0.5Zn and Mg-3.5Li-4Zn alloy samples there were a lot of corrosion products aggregated at 3 d. After 20 d immersion, however, the surfaces changed. Mg-3.5Li-0.5Zn alloy sample had a thick coating layer mainly composed of Mg, O and C, whilst the corrosion products on the surface of Mg-3.5Li-4Zn alloy sample were globular. On the cross-section, pure Mg sample showed typical characteristics of pitting corrosion through the surface layer, together with the formation of corrosion products. Mg-3.5Li-2Zn sample exhibited a much clearer and uniform corrosion layer, as compared with pure Mg sample, which was considered to be the result of a change in corrosion mechanism. Despite similar macroscopic local corrosion morphologies between Mg-3.5Li-2Zn and the other Mg-Li-Zn alloys (Figure S2), the cross-section of Mg-3.5Li-2Zn sample had much shallower corrosion beneath the surface, as compared

with the other alloy samples that suffered from severer local corrosion. For Mg-3.5Li-0.5Zn, a few severe corrosion sites were visible, as shown in Figure 5, and loose corrosion products of large amounts were composed mainly of Mg and O (data not shown). The visible holes in the corrosion products indicated the possibility of the penetration of Cl^- and other ions. By comparison, the corrosion layer of Mg-3.5Li-4Zn alloy sample showed a flake-like structure with open space for ion penetration. Surprisingly, Mg-6.5Li-xZn alloy samples exhibited a similar trend to Mg-3.5Li-xZn alloy samples. Mg-6.5Li-2Zn alloy sample had a shallow corrosion layer on the surface, whereas Mg-6.5Li-0.5Zn and Mg-6.5Li-4Zn alloy samples showed the penetration of corrosion from the surface.

Figure 6 shows the surface chemistry of Mg-Li-Zn alloy samples after 20 d immersion. The infrared spectra of the involved functional groups are shown in Figure 6a. The results revealed the presence of CO_3^{2-} and PO_4^{3-} (and/or HPO_4^{2-}) in the corroded area on the surface. In fact, it was hard to distinguish the functional groups over a certain range of wavenumbers. The defined 830-890 cm^{-1} wavenumber range has been reported to be the CO_3^{2-} (v_2) band [26-28], but other reports have shown the IR band of HPO_4^{2-} in a similar range [29, 30]. Furthermore, an overlapping range of 960-1150 cm^{-1} between PO_4^{3-} and HPO_4^{2-}[31-33] has been reported. Further XRD investigation confirmed the presence of $Mg(OH)_2$ as well as $MgCO_3$, as shown in Figure 6b. The dashed line and circled peaks in Figure 6b might indicate the presence of $MgHPO_4 \cdot 3H_2O$ (newberyite) and/or $Mg_3(PO_4)_2$ since no other peaks at low 2θ angles were found. Further XPS results proved the existence of Mg, O, C and P in the corrosion products. High resolution narrow scan confirmed the presence of $MgCO_3$ and $Mg(OH)_2$, and the detected peaks were in good agreement with the findings given in the literature. P showed a single peak at 133.6 eV. Based on the information in the literature, this peak might be related either to PO_4^{3-} [34, 35]

or to HPO_4^{2-} [36], which made the P-containing compound uncertain. Nevertheless, no Ca was detected from XPS.

3.6 Cell morphology, cell viability assay and NO release

Cell morphologies of VSMCs cultured in different extracts are shown in Figure 7a. VSMCs showed benign responses to all the tested materials at 24 h and had good spreading morphologies in numerous directions, as well as good cell-to-cell connection and visible stained cytoplasmic filament. However, the viability of VSMCs cultured in the extracts continuously decreased with time (Figure 7c). This suggests a continuing and lagged response of VSMCs. Previous cytotoxicity tests also indicated the toxicity of Mg-Li-based materials for VSMCs [12]. Ion concentrations in the DMEM extracts were determined (Figure 7e). The results showed lower amounts of released Mg^{2+} in all the Mg-Li-Zn alloy extracts except that of the Mg-3.5Li-4Zn alloy, as compared with those in pure Mg extracts, implying relative better corrosion resistance of the Mg-Li-Zn alloys in the cell culture environment. Cell morphologies of HUVECs cultured in different extracts for 24 h are shown in Figure 7b. The cultured cells presented healthy squamous morphologies like those cultured in the culture medium. Furthermore, the 5 d results indicated that the ion concentrations as well as the pH values were tolerable for HUVECs, which is different from the results from the viability assay of VSMCs (compare Figure 7c with Figure 7d).

Nitric oxide (NO) has been widely accepted as endothelium-derived relaxing factor (EDRF) to relax the surrounding smooth muscle [37], inhibit the growth of VSMCs and reduce the chances of thrombosis and restenosis [38]. The NO release results revealed significant increases of NO in all the Mg-Li-Zn alloy extracts except that of Mg-3.5Li-0.5Zn. Apart from the Mg-Li-Zn alloys, pure Mg also showed increased NO release, which is in good agreement with the findings

obtained from the previous research [39]. The increased NO release, as shown in Figure 7f, provided evidence related to the continuing decrease of VSMC viability. Another interesting finding is that the Li-abundant Mg-Li-Zn alloys (i.e., Mg-6.5Li-0.5Zn, Mg-6.5Li-2Zn and Mg-6.5Li-4Zn) released nearly double amounts of NO, as compared with the negative control, which implied the potential improving effects on NO release of Li in the developed Mg-Li-Zn alloys.

3.7 Platelet adhesion and hemolysis

Hemocompatibility test results of Mg-Li-Zn alloys are shown in Figure 8. In theory, aggregation begins after activation [40]. Pure Mg showed obvious aggregation of human platelets with some platelets having extended pseudopodia. The Mg-Li-Zn alloys caused different degrees of aggregation of the platelets. By comparison, the Mg-3.5Li-2Zn alloy showed less aggregation, which happened in only two or three platelets. Besides, most of the platelets remained separated and round (Figure 8c). It is worth noting that the platelets adhered on the surface of the Mg-6.5Li-2Zn alloy showed an apparent transition morphology (Figure 8f). A few platelets aggregated but most of the platelets extended pseudopodia for further aggregation, indicating a state of induction. For all the materials, a corroded surface with proteins could be easily observed underneath the platelets, as a result of immersion in Platelet-Rich Plasma (PRP). However, the Mg-3.5Li-2Zn alloy appeared to show a smaller amount of protein on the surface, with corrosion crack occurring only on the surface, which might contribute to the relatively better hemolysis. Furthermore, released NO can provide another function to reduce the adhesion and activation of platelets in addition to inhibiting the proliferation of VSMCs [41]. The present results suggest good hemocompatibility of the currently investigated Mg-Li-Zn alloys in vitro, which calls for in vivo evaluation for verification. Hemolysis results are shown in Figure 8h. Only the Mg-3.5Li-2Zn alloy had a hemolysis value lower than 5%. This result is easily understandable because the

18

hemolysis of biodegradable Mg alloys is strongly dependent on corrosion resistance and related ion release and pH change.

3.8 Coagulation four

Four common clinical indexes including activated partial thromboplastin time (APTT), prothrombin time (PT), Fibrinogen with Clauss method (FIB-C) and thrombin time (TT) are shown in Figure 9. APTT and PT are used to show the speed of coagulation caused by intrinsic coagulation pathway and extrinsic coagulation pathway, respectively. Fibrinogen is a glycoprotein in vertebrates that helps in the formation of blood clots, whilst TT measures the time of clot formation in the plasma of a blood sample containing anticoagulant [42], or known as thrombin-mediated fibrin formation [43]. All the four indexes stayed in a range for healthy people. Pure Mg, Mg-3.5Li-0.5Zn, Mg-3.5Li-2Zn and all the Mg-6.5Li-xZn alloys showed significant increases of APTT relative to the control, indicating the effects of these materials on the intrinsic pathway. Furthermore, the increased amounts of alloying elements showed a tendency of prolonged APTT results, suggesting the effects of Li^+ and Zn^{2+} in the prolonged APTT. The results were in good agreement with those obtained in a previous study where Zn^{2+} influenced the intrinsic pathway by binding to factor XII [44]. Besides, all the APTT results were lower than 34 s, which would lead to no abnormal clinical effects [45]. As for PT, pure Mg had a significantly lower value than the negative control, implying pure Mg affected the extrinsic clotting pathway but all the Mg-Li-Zn alloys appeared to exert no influence. Fibrinogen before and after incubating the materials revealed no significant differences. As for TT, both Mg-3.5Li-2Zn and Mg-6.5Li-4Zn showed significant increases, as compared with the negative control group. For coagulation, the intracellular Ca^{2+} has been demonstrated to be critically involved in the functioning of coagulation cascade [46]. In this case, Mg^{2+}, as an antagonist to Ca^{2+}, would

delay the coagulation time [47]. Previous studies showed the tendency that Mg alloys with higher corrosion rates induced more delayed coagulation time [43, 48]. In this study, the coagulation time seemed be related to not only corrosion rate but also the ions released, since some of the alloys with higher corrosion rates showed less interference, as well as the tendency in the delayed time with the addition of alloying elements.

4. Discussion

4.1 Mechanical properties

As for the room-temperature mechanical properties, a summary of binary Mg-Li alloys and ternary Mg-Li-X (X=Al, Zn, Ca, Y, Ce) alloys is shown in Figure 10 [1, 11, 49-66]. It is obvious that the mechanical properties of magnesium are significantly improved by the addition of Li and Zn. Moreover. Zn shows the best strengthening effect, as compared with the other alloying elements, such as Ca, Y and Ce. Although aluminum has a good strengthening effect in Mg-Li-Al alloys, it is potentially neurotoxic. Thus, our results confirm that Zn is indeed an effective element to replace aluminum to achieve a good balance between strength and ductility. As far as the choice of material for potential stent application is concerned, the Mg-3.5Li-2Zn alloy (~250 MPa UTS, >20% elongation) is superior to other alloys currently studied and previously studied, including Mg-Li or Mg-Li-X alloys subjected to ECAP (equal channel angular pressing) or other post-processing [1, 54, 60, 62-67], and including the Mg-Li-Ca alloys previously developed for biomedical applications [11]. Obviously, any medical devices potentially made of the Mg-Li-Zn alloys will have distinct advantages in specific strength and exceptionally large ductility as needed for vascular stents.

4.2 Biodegradation behavior

On the surface of the alloys studied, Li_2CO_3 is present in the protecting layer. Moreover, at a low Li content, the concentrations of Li and Mg on the surface seem to be adjustable by the content of Zn. The Mg-3.5Li-2Zn and Mg-3.5Li-4Zn alloys show higher concentrations of Mg and lower concentrations of Li on the surface, whilst the Mg-3.5Li-0.5Zn alloy has a higher Li concentration on the surface. Besides, the corrosion mechanism changes with increasing amounts of Li and Zn, which is reported for the first time. With increasing Zn content from 0.5 to 4 wt.%, the corrosion mechanism changes from local corrosion with a few pitting sites, to local corrosion with small pitting, and to severe local corrosion (Figure S2). Furthermore, with the addition of Li and Zn, naturally oxidized Mg-Li-Zn alloys have different corrosion preferences, which is shown in Figure S3.

The reported Mg-Li-based alloys for biomedical applications include the Mg-Li-(Al)-(RE) alloys [12], Mg-Li-Ca alloys [11] and Mg-Li-Zn alloys in the present study. Specifically, the as-cast and as-extruded Mg-9.29Li-0.88Ca alloy was subjected to short immersion tests up to 430 min and had the corrosion rates 1.22 $ml·cm^{-2}·d^{-1}$ and 0.702 $ml·cm^{-2}·d^{-1}$, respectively, determined from hydrogen evolution. Thus, the amounts of evolved hydrogen after 430 min were calculated to be 0.3643 $ml·cm^{-2}$ and 0.2096 $ml·cm^{-2}$, respectively. Comparison in hydrogen evolution after 240 h between the Mg-Li-(Al)-(RE) alloys and the alloys used in the present study is shown in Figure 11a. It is obvious that the Mg-Li-Zn alloys developed in this study have overall better corrosion resistance in Hank's solution. Corrosion current density shows the transient behavior of metals with time. It is therefore interesting to compare the corrosion current density values of the Mg-Li-(Al)-(RE) alloys, Mg-9.29Li-0.88Ca alloy and the alloys used in the present study. It is obvious that the corrosion current density values of the alloys used in the present study are

21

among the lowest ones, although the determination of the Tafel slope may cause large variations [18].

4.3 In vitro cytocompatibility

The HUVEC viability assay in the present study suggests the viability of cells cultured in extracts is first suppressed but then return to normal. The slight suppressing on day one may be considered to be caused by a relatively high pH value, since the concentration level of either Mg^{2+} or Li^+ will not cause the HUVEC viability to suppress [68]. The maximal concentration of Mg^{2+} that does not inhibit the viability of HCAECs (Human coronary aorta endothelial cells) has been found to be 30 mM, which corresponds to nearly 700 mg·L^{-1} [69]. This value is much larger than Mg^{2+} concentrations encountered in this study. As for the VSMC viability, a low level of magnesium ion concentration (below 40 mM) has been found to show no side effects on human VSMCs [70] and again this value is much larger than the Mg^2+ concentrations encountered in this study. The extracts obtained in this study except that for Mg-3.5Li-0.5Zn all had Li^+ concentrations around 1 mM. In the previous research, 5 mM LiCl was found to suppress the proliferation of rat VSMCs [71] but lower Li^+ content could affect the cells. In the present study, it is not certain if the Li^+ concentration alone has a toxic effect on VSMCs at 5 d. In addition to Li^+ concentration, the alkaline environment caused by the biodegradation of magnesium may affect the cell viability. Moreover, a relationship between increasing NO release and increasing Li^+ release has been found. This needs further investigation. All in all, the current study proves the in vitro biosafety of the Mg-Li-Zn alloys.

5． Conclusions

In this study, Mg-Li-Zn alloys were investigated to explore the feasibility to use these alloys as potential biodegradable stent materials. The results showed enhanced mechanical properties (both strength and ductility, relative to pure magnesium), good corrosion resistance and good biocompatibility, indicating the potential of the Mg-Li-Zn alloys as good candidates for cardiovascular stent application. The main findings are as follows.

(1) A protecting surface layer containing Li_2CO_3/$MgCO_3$ was formed on the alloy surface, which was dependent on the Li/Mg ratio of the alloy. Zn seemed to be located along the β-phase and was not detected in the protecting layer.

(2) The Mg-Li-Zn alloys exhibited significantly improved mechanical properties. The Mg-3.5Li-2Zn alloy developed in the present study showed superior mechanical properties to most of reported binary Mg-Li and ternary Mg-Li-X (X=Al, Zn, Ca, Y, Ce, Sc, Mn and Ag) alloys.

(3) Both electrochemical tests and in vitro corrosion evaluation showed comparable corrosion resistance of Mg-3.5Li-2Zn and Mg-6.5Li-2Zn to that of pure Mg in Hank's solution and superior corrosion resistance in the cell culture medium. The corrosion products were found to be composed of $Mg(OH)_2$, $MgCO_3$ and Ca-free Mg/P inorganics and Ca/P inorganics.

(4) In vitro cytotoxicity assay revealed different behaviors of HUVECs and VSMCs. HUVECs showed increased NO release and tolerable toxicity, while VSMCs had continuingly decreased viability with time.

(5) Hemocompatibility tests showed different degrees of activation behavior of the Mg-Li-Zn alloys and the hemolysis of Mg-3.5Li-2Zn was lower than 5%. Further coagulation four results showed good reaction of PPP to the Mg-Li-Zn alloys.

References

[1] Chang T-C, Wang J-Y, Chu C-L, Lee S. Mechanical properties and microstructures of various Mg–Li alloys. Materials Letters 2006;60:3272-6.

[2] Agnew SR, Yoo MH, Tomé CN. Application of texture simulation to understanding mechanical behavior of Mg and solid solution alloys containing Li or Y. Acta Materialia 2001;49:4277-89.

[3] Song Y, Shan D, Chen R, Han E-H. Corrosion characterization of Mg–8Li alloy in NaCl solution. Corrosion Science 2009;51:1087-94.

[4] Cao D, Wu L, Sun Y, Wang G, Lv Y. Electrochemical behavior of Mg–Li, Mg–Li–Al and Mg–Li–Al–Ce in sodium chloride solution. JPS 2008;177:624-30.

[5] Xu W, Birbilis N, Sha G, Wang Y, Daniels JE, Xiao Y, et al. A high-specific-strength and corrosion-resistant magnesium alloy. Nature materials 2015;14:1229-35.

[6] Geddes JR, Burgess S, Hawton K, Jamison K, Goodwin GM. Long-term lithium therapy for bipolar disorder: systematic review and meta-analysis of randomized controlled trials. Am J Psychiatry 2004;161:217-22.

[7] Kean S. The disappearing spoon and other true tales of madness, love, and the history of the world from the periodic table of the elements. Tce the Chemical Engineer 2011;135:102-.

[8] Lieb J, Zeff A. Lithium treatment of chronic cluster headaches. Br J Psychiatry 1978;133:556-8.

[9] Guo S, Arai K, Stins MF, Chuang DM, Lo EH. Lithium upregulates vascular endothelial growth factor in brain endothelial cells and astrocytes. Stroke 2009;40:652-5.

[10] Ghasemi M, Dehpour AR. The NMDA receptor/nitric oxide pathway: a target for the therapeutic and toxic effects of lithium. Trends Pharmacol Sci 2011;32:420-34.

[11] Zeng R-C, Sun L, Zheng Y-F, Cui H-Z, Han E-H. Corrosion and characterisation of dual phase Mg–Li–Ca alloy in Hank's solution: The influence of microstructural features. Corrosion Science 2014;79:69-82.

[12] Zhou WR, Zheng YF, Leeflang MA, Zhou J. Mechanical property, biocorrosion and in vitro biocompatibility evaluations of Mg-Li-(Al)-(RE) alloys for future cardiovascular stent application. Acta Biomater 2013;9:8488-98.

[13] Hambidge KM, Krebs NF. Zinc Deficiency: A Special Challenge. The Journal of Nutrition 2007;137:1101-5.

[14] Bowen PK, Drelich J, Goldman J. Zinc exhibits ideal physiological corrosion behavior for bioabsorbable stents. Advanced materials 2013;25:2577-82.

[15] Zhao S, McNamara CT, Bowen PK, Verhun N, Braykovich JP, Goldman J, et al. Structural Characteristics and In Vitro Biodegradation of a Novel Zn-Li Alloy Prepared by Induction Melting and Hot Rolling. Metallurgical and Materials Transactions A 2017;48:1204-15.

[16] Gu X, Zheng Y, Cheng Y, Zhong S, Xi T. In vitro corrosion and biocompatibility of binary magnesium alloys. Biomaterials 2009;30:484-98.

[17] Zhang S, Zhang X, Zhao C, Li J, Song Y, Xie C, et al. Research on an Mg–Zn alloy as a degradable biomaterial. Acta Biomater 2010;6:626-40.

[18] Kirkland NT, Birbilis N, Staiger MP. Assessing the corrosion of biodegradable magnesium implants: a critical review of current methodologies and their limitations. Acta Biomater 2012;8:925-36.

[19] Zeng RC, Cui LY, Jiang K, Liu R, Zhao BD, Zheng YF. In Vitro Corrosion and Cytocompatibility of a Microarc Oxidation Coating and Poly(L-lactic acid) Composite Coating on Mg-1Li-1Ca Alloy for Orthopedic Implants. ACS applied materials & interfaces 2016;8:10014-28.

[20] Eriksson T, Andersson AM, Bishop AG, Gejke C, Gustafsson TR, Thomas JO. Surface Analysis of LiMn2 O 4 Electrodes in Carbonate-Based Electrolytes. Journal of the Electrochemical Society 2002;149:A69-A78.

[21] Garg KB, Chatterji T, Dalela S, Heinonnen M, Leiro J, Dalela B, et al. Core level photoemission study of polycrystalline MgB2. SSCom 2004;131:343-7.

[22] Bouvier Y, Mutel B, Grimblot J. Use of an Auger parameter for characterizing the Mg chemical state in different materials. Surface and Coatings Technology 2004;180–181:169-73.

[23] Tanaka S, Taniguchi M, Tanigawa H. XPS and UPS studies on electronic structure of Li2O. JNuM 2000;283–287, Part 2:1405-8.

[24] Kang WL, Lee B, Kang HJ, Da YK, Kim JI, Kwon DY, et al. Biodegradable stent. Journal of Biomedical Science & Engineering 2012;05.

[25] Haynes, William M. CRC handbook of chemistry and physics: CRC Press, Inc; 2010.

[26] Bowen PK, Drelich J, Goldman J. Magnesium in the murine artery: probing the products of corrosion. Acta Biomater 2014;10:1475-83.

[27] Lebon M, Reiche I, Fröhlich F, Bahain J-J, Falguères C. Characterization of archaeological burnt bones: contribution of a new analytical protocol based on derivative FTIR spectroscopy and curve fitting of the ν 1 ν 3 PO4 domain. Anal Bioanal Chem 2008;392:1479-88.

[28] Brangule A, Agris Gross K. Importance of FTIR Spectra Deconvolution for the Analysis of Amorphous Calcium Phosphates. Materials Science & Engineering 2015;77.

[29] Victoria EC, Gnanam F. Synthesis and characterization of biphasic calcium phosphate. Trends Biomater Artif Organs 2002;16:12-4.

[30] Boonchom B. Kinetic and thermodynamic studies of MgHPO4· 3H2O by non-isothermal decomposition data. JTAC 2009;98:863-71.

[31] Lebon M, Reiche I, Fröhlich F, Bahain J-J, Falguères C. Characterization of archaeological burnt bones: contribution of a new analytical protocol based on derivative FTIR spectroscopy and curve fitting of the ν 1 ν 3 PO4 domain. Anal Bioanal Chem 2008;392:1479-88.

[32] Leung Y, Walters MA, Legeros RZ. Second derivative infrared spectra of hydroxyapatite. Spectrochimica Acta Part A Molecular Spectroscopy 1990;46:1453–9.

[33] Paschalis EP, Dicarlo E, Betts F, Sherman P, Mendelsohn R, Boskey AL. FTIR microspectroscopic analysis of human osteonal bone. Calcif Tissue Int 1996;59:480-7.

[34] Chang WH, Qu B, Liao AD, Zhang SF, Zhang RF, Xiang JH. In vitro biocompatibility and antibacterial behavior of anodic coatings fabricated in an organic phosphate containing solution on Mg–1.0Ca alloys. Surface and Coatings Technology 2016;289:75-84.

[35] Zhu X, Chen J, Scheideler L, Reichl R, Geis-Gerstorfer J. Effects of topography and composition of titanium surface oxides on osteoblast responses. Biomaterials 2004;25:4087-103.

[36] Barrère F, Lebugle A. Calcium phosphate interactions with titanium oxide and alumina substrates: an XPS study. Journal of Materials Science: Materials in Medicine 2003;14:419-25.

[37] Palmer RM, Ashton DS, Moncada S. Vascular endothelial cells synthesize nitric oxide from L-arginine. Nature 1988;333:664-6.

[38] Bohl KS, West JL. Nitric oxide-generating polymers reduce platelet adhesion and smooth muscle cell proliferation. Biomaterials 2000;21:2273-8.

[39] Wang G, Ge S, Shen Y, Wang H, Dong Q, Zhang Q, et al. Study on the biodegradability and biocompatibility of WE magnesium alloys. Materials Science and Engineering: C 2012;32:2190-8.

[40] Yip J, Yang S, Berndt MC, Andrews RK. Primary Platelet Adhesion Receptors. IUBMB Life 2005;57:103-8.

[41] Loscalzo J. Nitric Oxide and Restenosis. Clin Appl Thromb Hemost 1996;2:7-10.

[42] Key N, Makris M, O'Shaughnessy D, Lillicrap D. Practical hemostasis and thrombosis: Wiley Online Library; 2009.

[43] Wang J, He Y, Maitz MF, Collins B, Xiong K, Guo L, et al. A surface-eroding poly(1,3-trimethylene carbonate) coating for fully biodegradable magnesium-based stent applications: toward better biofunction, biodegradation and biocompatibility. Acta Biomater 2013;9:8678–89.

[44] Schousboe I. Contact activation in human plasma is triggered by zinc ion modulation of factor XII (Hageman factor). Blood Coagul Fibrinolysis 1993;4:671-8.

[45] Scarpelini S, Rhind S, Nascimento B, Tien H, Shek P, Peng H, et al. Normal range values for thromboelastography in healthy adult volunteers. Brazilian journal of medical and biological research 2009;42:1210-7.

[46] Daniel JL, Dangelmaier C, Jin J, Ashby B, Smith JB, Kunapuli SP. Molecular basis for ADP-induced platelet activation I. Evidence for three distinct ADP receptors on human platelets. J Biol Chem 1998;273:2024-9.

[47] Adams J, Mitchell J. The effect of agents which modify platelet behaviour and of magnesium ions on thrombus formation in vivo. Thromb Haemost 1979;42:603-10.

[48] Lu P, Cao L, Liu Y, Xu X, Wu X. Evaluation of magnesium ions release, biocorrosion, and hemocompatibility of MAO/PLLA‐modified magnesium alloy WE42. Journal of Biomedical Materials Research Part B: Applied Biomaterials 2011;96:101-9.

[49] Wang JY, Chang TC, Chang LZ, Lee S. Effect of Al and Mn Content on the Mechanical Properties of Various ECAE Processed Mg-Li-Zn Alloys. Materials Transactions 2006;47:971-6.

[50] Takuda H, Kikuchi S, Tsukada T, Kubota K, Hatta N. Effect of strain rate on deformation behaviour of a Mg–8.5Li–1Zn alloy sheet at room temperature. Materials Science & Engineering A 1999;271:251-6.

[51] Dong H, Wang L, Wu Y, Wang L. Effect of Y on microstructure and mechanical properties of duplex Mg–7Li alloys. Journal of Alloys & Compounds 2010;506:468-74.

[52] Wu R, Qu Z, Zhang M. Effects of the addition of Y in Mg–8Li–(1,3)Al alloy. Materials Science & Engineering A 2009;516:96-9.

[53] Dong H, Pan F, Jiang B, Zeng Y. Evolution of microstructure and mechanical properties of a duplex Mg–Li alloy under extrusion with an increasing ratio. Materials & Design 2014;57:121-7.

[54] Lin Y-N, Wu H-Y, Zhou G-Z, Chiu C-H, Lee S. Mechanical and anisotropic behaviors of Mg–Li–Zn alloy thin sheets. Materials & Design 2008;29:2061-5.

[55] Sanschagrin A, Tremblay R, Angers R, Dubé D. Mechanical properties and microstructure of new magnesium—lithium base alloys. Materials Science & Engineering A 1996;220:69-77.

[56] Xu DK, Zu TT, Yin M, Xu YB, Han EH. Mechanical properties of the icosahedral phase reinforced duplex Mg–Li alloy both at room and elevated temperatures. Journal of Alloys & Compounds 2014;582:161-6.

[57] Zhang ML, Wu RZ, Wang T. Microstructure and mechanical properties of Mg–8Li–(0–3)Ce alloys. Journal of Materials Science 2009;44:1237-40.

[58] Crawford P, Barrosa R, Mendez J, Foyos J, Es-Said OS. On the transformation characteristics of LA141A (Mg-Li-Al) alloy. Journal of Materials Processing Technology 1996;56:108-18.

[59] Kubota K, Mabuchi M, Higashi K. Review Processing and mechanical properties of fine-grained magnesium alloys. Journal of Materials Science 1999;34:2255-62.

[60] Takuda H, Matsusaka H, Kikuchi S, Kubota K. Tensile properties of a few Mg-Li-Zn alloy thin sheets. Journal of Materials Science 2002;37:51-7.

[61] Liu T, Wang YD, Wu SD, Peng RL, Huang CX, Jiang CB, et al. Textures and mechanical behavior of Mg–3.3%Li alloy after ECAP. Scripta Materialia 2004;51:1057-61.

[62] Takuda H, Enami T, Kubota K, Hatta N. The formability of a thin sheet of Mg–8.5Li–1Zn alloy. Journal of Materials Processing Technology 2000;101:281-6.

[63] Karami M, Mahmudi R. Work hardening behavior of the extruded and equal-channel angularly pressed Mg–Li–Zn alloys under tensile and shear deformation modes. Materials Science and Engineering: A 2014;607:512-20.

[64] Guiying, Sha, Xiaoguang, Teng, Liu, Yuhong, et al. Effects of Sc Addition and Annealing Treatment on the Microstructure and Mechanical Properties of the As-rolled Mg-3Li alloy. Journal of Materials Science & Technology 2011;27:753-8.

[65] Hong-Bin LI, Hai-Bin JI, Yao GC, Liu YH, Guo ZQ. Microstructure and Mechanical Properties of Mg-Li-Mn Alloy. Chinese Journal of Process Engineering 2006;6:491-4.

[66] Zhang M, F.M.Elkin. Mg-Li ultra-light alloy (in Chinese): Science Press; 2010.

[67] Jones WRD, Hogg GV. The stability of mechanical properties of beta-phase magnesium-lithium alloys. Jinstmetals 1957;85.

[68] Feyerabend F, Fischer J, Holtz J, Witte F, Willumeit R, Drucker H, et al. Evaluation of short-term effects of rare earth and other elements used in magnesium alloys on primary cells and cell lines. Acta biomaterialia 2010;6:1834-42.

[69] Zhao N, Zhu D. Endothelial responses of magnesium and other alloying elements in magnesium-based stent materials. Metallomics Integrated Biometal Science 2014;7:118-28.

[70] Ma J, Zhao N, Zhu D. Biphasic responses of human vascular smooth muscle cells to magnesium ion. Journal of Biomedical Materials Research Part A 2016;104:347-56.

[71] Wang Z, Zhang X, Chen S, Wang D, Wu J, Liang T, et al. Lithium chloride inhibits vascular smooth muscle cell proliferation and migration and alleviates injury-induced neointimal hyperplasia via induction of PGC-1α. PloS one 2013;8:e55471-e.

Table captions

Table 1. Analyzed compositions of the Mg-Li-Zn alloys used in the present study.

Table 2. Open circuit potential, corrosion potential (E_{corr}), corrosion current density (I_{corr}) and corrosion rate values obtained from the electrochemical tests.

Table.1

Nominal composition (wt.%)	Analyzed composition (wt.%)		
	Li	Zn	Mg
Mg-3.5Li-0.5Zn	3.69±0.13	0.51±0.04	Balance
Mg-3.5Li-2Zn	3.72±0.05	2.26±0.17	Balance
Mg-3.5Li-5Zn	3.64±0.06	4.38±0.06	Balance
Mg-6.5Li-0.5Zn	6.15±0.18	0.81±0.04	Balance
Mg-6.5Li-2Zn	6.75±0.12	2.13±0.10	Balance
Mg-6.5Li-4Zn	6.83±0.08	3.47±0.11	Balance

Table. 2

	Open circuit potential (V_{SCE})	E_{corr} (V_{SCE})	I_{corr} ($\mu A \cdot cm^{-2}$)	Corrosion rate (mm·y^{-1})
Pure Mg	-(1.634±0.042)	-(1.556±0.010)	7.764±0.638	0.176±0.014
Mg-3.5Li-0.5Zn	-(1.612±0.029)	-(1.554±0.044)	15.140±1.125	0.343±0.025
Mg-3.5Li-2Zn	-(1.623±0.005)	-(1.590±0.001)	10.616±0.304	0.241±0.007
Mg-3.5Li-4Zn	-(1.577±0.001)	-(1.543±0.005)	13.920±1.754	0.315±0.040
Mg-6.5Li-0.5Zn	-(1.610±0.006)	-(1.562±0.032)	14.888±2.933	0.337±0.066
Mg-6.5Li-2Zn	-(1.593±0.009)	-(1.546±0.006)	13.110±0.159	0.297±0.004
Mg-6.5Li-4Zn	-(1.608±0.023)	-(1.566±0.012)	12.443±0.663	0.282±0.015

Figure captions

Figure 1. (a) Microstructures of Mg-3.5Li-0.5Zn, Mg-3.5Li-2Zn, Mg-3.5Li-4Zn, Mg-6.5Li-0.5Zn, Mg-6.5Li-2Zn, and Mg-6.5Li-4Zn, with red arrows pointing to representative particles, (b) XRD results and (c) the presence of Zn-containing particles.

Figure 2. XPS spectra of (a) Mg-3.5Li-2Zn and (b) Mg-6.5Li-2Zn.

Figure 3. Yield strength (YS), ultimate tensile strength (UTS) and elongation values of the Mg-Li-Zn alloys.

Figure 4. (a) Potentiodynamic polarization, (b) total hydrogen evolution, (c) pH value of Hank's solution and (d) ion concentrations of Hank's solution at 20 d with pure Mg as the control.

Figure 5. Surface morphologies, elements detected at 3 and 20 d, and the morphologies of corrosion products on the cross section at 20 d.

Figure 6. Characterization of surface chemistry after 20 d immersion. (a) FTIR files, (b) XRD results of Mg-3.5Li-4Zn and Mg-6.5Li-4Zn, (c) XPS results of the corrosion products on Mg-6.5Li-4Zn with high resolution XPS files of C, O, Mg and P (no Ca found from XPS).

Figure 7. Actin-nucleus co-staining of (a) VSMC morphologies and (b) HUVEC morphologies after 24 h in the extracts. (c) VSMC viability, (d) HUVEC viability, (e) ion concentrations of DMEM extracts and (f) NO release of HUVECs cultured in extracts for 24 h.

Figure 8. Platelet adhesion on (a) pure Mg, (b) Mg-3.5Li-0.5Zn, (c) Mg-3.5Li-2Zn, (d) Mg-3.5Li-4Zn, (e) Mg-6.5Li-0.5Zn, (f) Mg-6.5Li-2Zn, and (g) Mg-6.5Li-4Zn and (h) hemolysis rate. The scale bar in the zoomed image is 2 μm.

Figure 9. APTT, PT, FIB-C and TT results of samples incubated in platelet-poor plasma (PPP)

Figure 10. Summary of room temperature mechanical properties of binary Mg-Li alloys and ternary Mg-Li-X (X=Al, Zn, Ca, Y, Ce, Sc, Mn, Ag) alloys [1, 11, 49-66].

Figure 11. Comparison in (a) hydrogen evolution between the previously studied Mg-Li-(Al)-(RE) alloys and the present Mg-Li-Zn alloys after 240 h immersion in Hank's solution at 37 °C, and (b) corrosion current density between the previously studied Mg-Li-Ca and Mg-Li-(Al)-(RE) alloys and the present Mg-Li-Zn alloys.

Figure S1. XPS spectra of Mg-3.5Li-0.5Zn (a)-(d), Mg-3.5Li-2Zn (e)-(f), Mg-6.5Li-0.5Zn (i)-(l) and Mg-6.5Li-2Zn (m)-(p)

Figure S2. Optical images of the corrosion behavior at 20 d of (a) the as-extruded Mg, (b) Mg-3.5Li-0.5Zn, (c) Mg-3.5Li-2Zn, (d) Mg-3.5Li-4Zn, (e) Mg-6.5Li-0.5Zn, (f) Mg-6.5Li-2Zn and (g) Mg-6.5Li-4Zn.

Figure S3. Naturally oxidized surfaces of Mg-3.5Li-2Zn (a)(b), Mg-6.5Li-2Zn (c), Mg-6.5Li-0.5Zn (d)(e) and EDS mapping on Mg-6.5Li-0.5Zn (f).
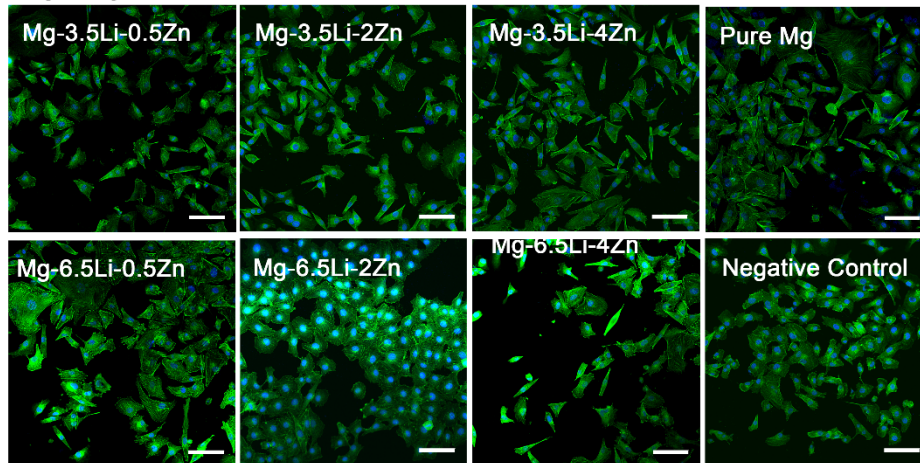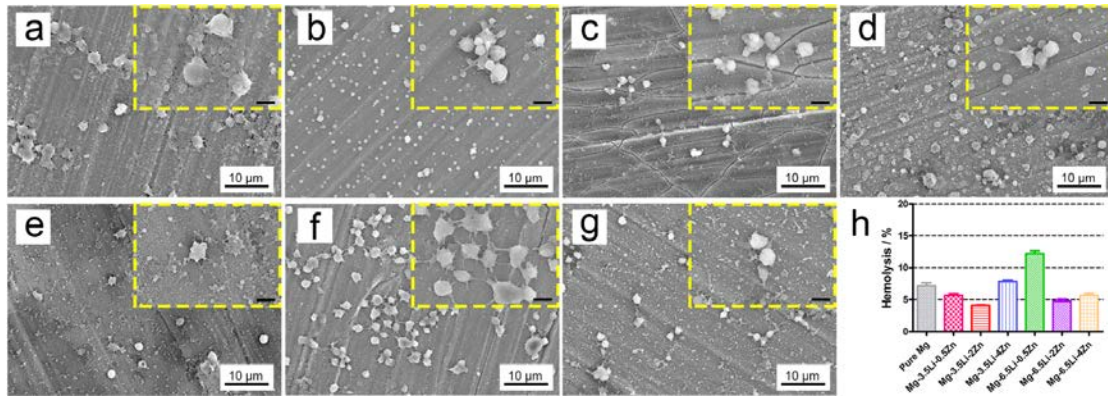
Fig.1
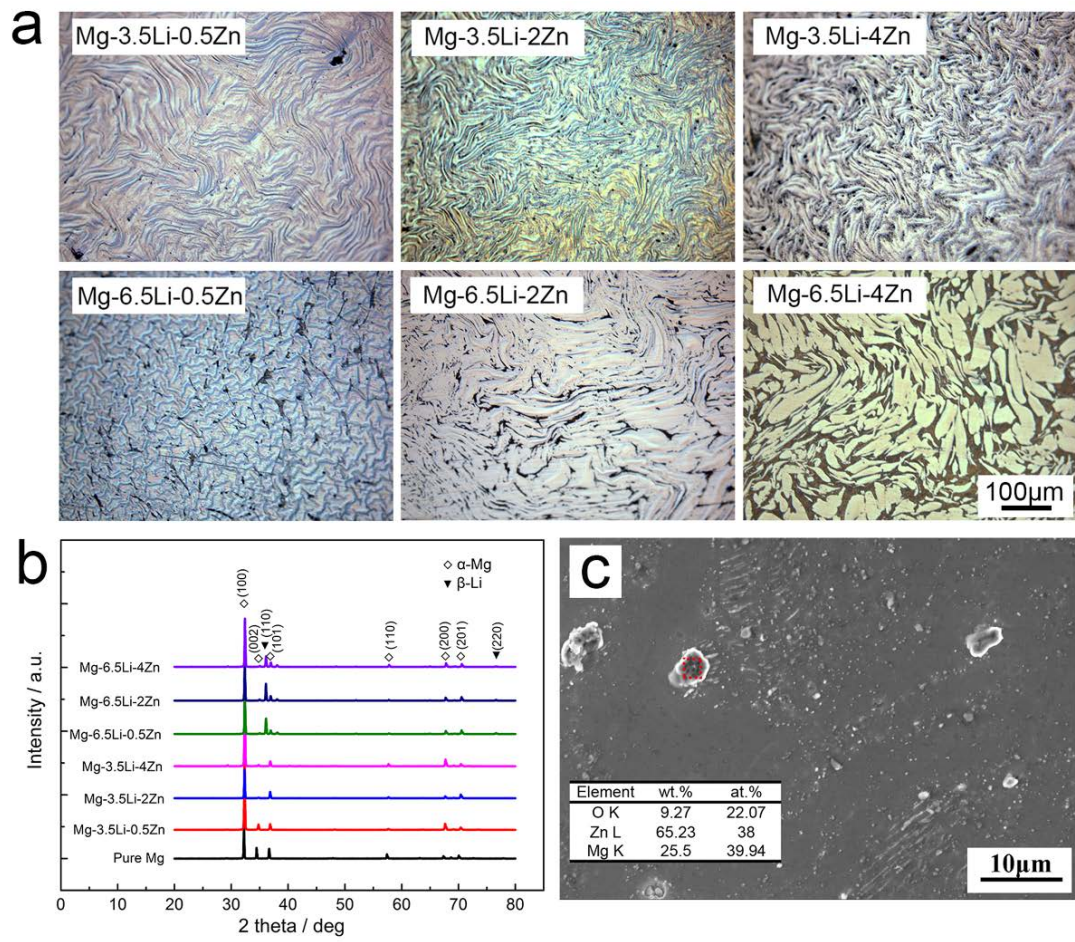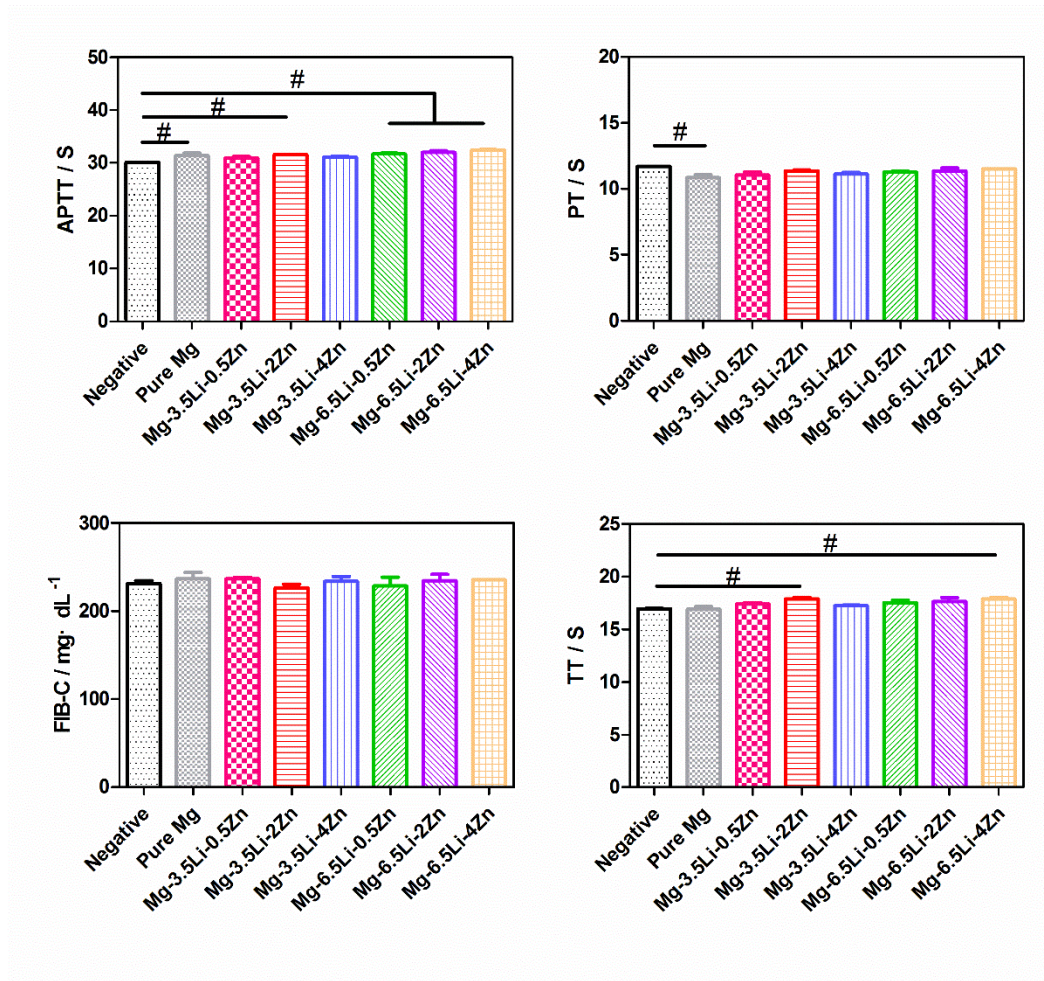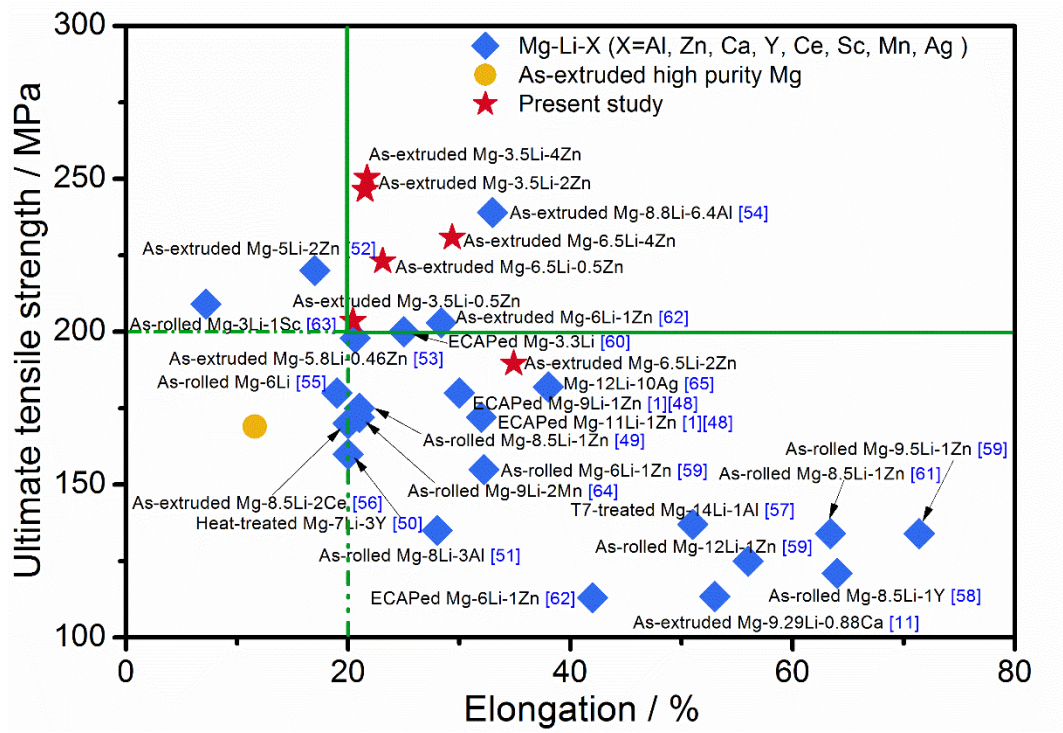
Fig.2
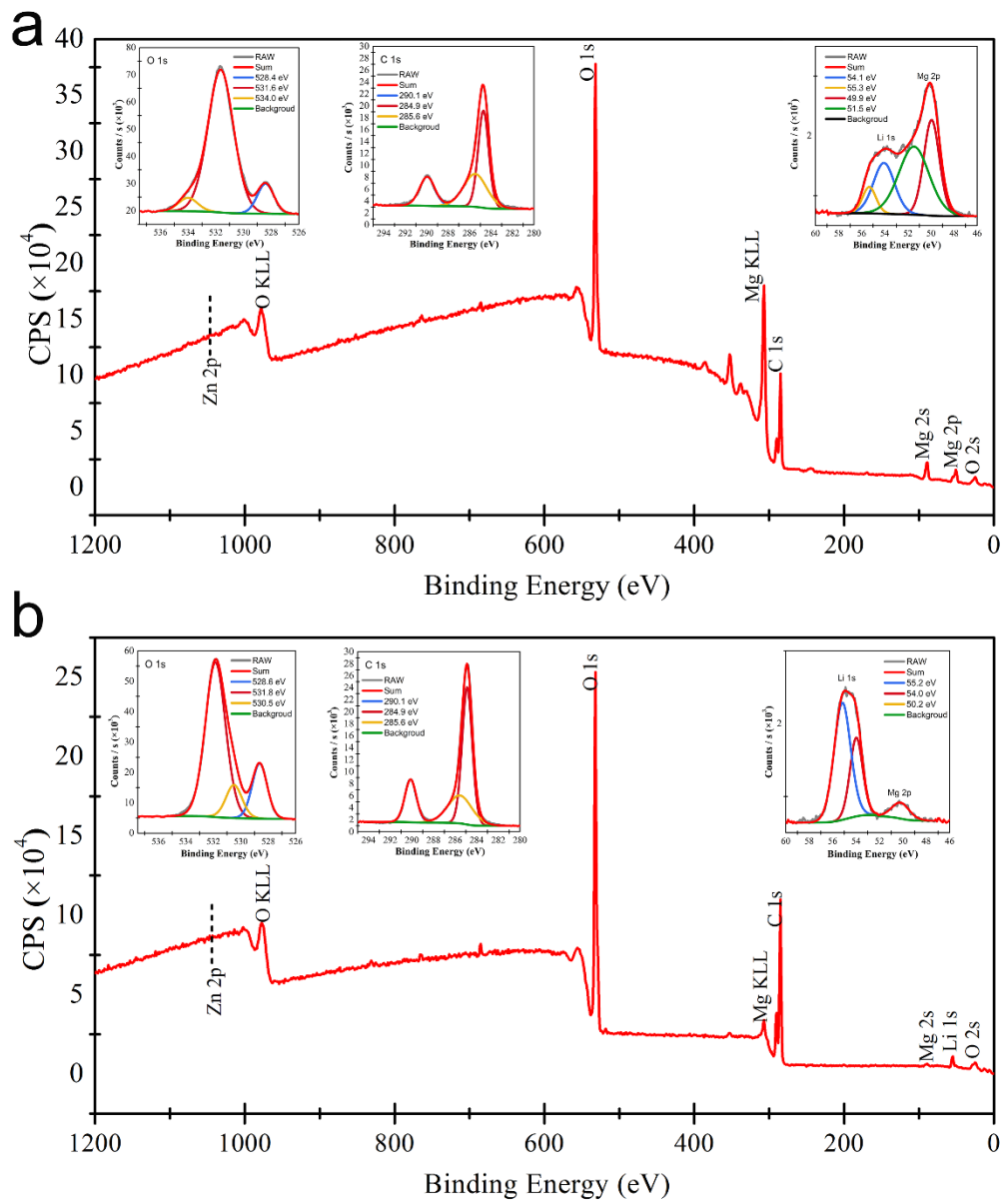
Fig.3
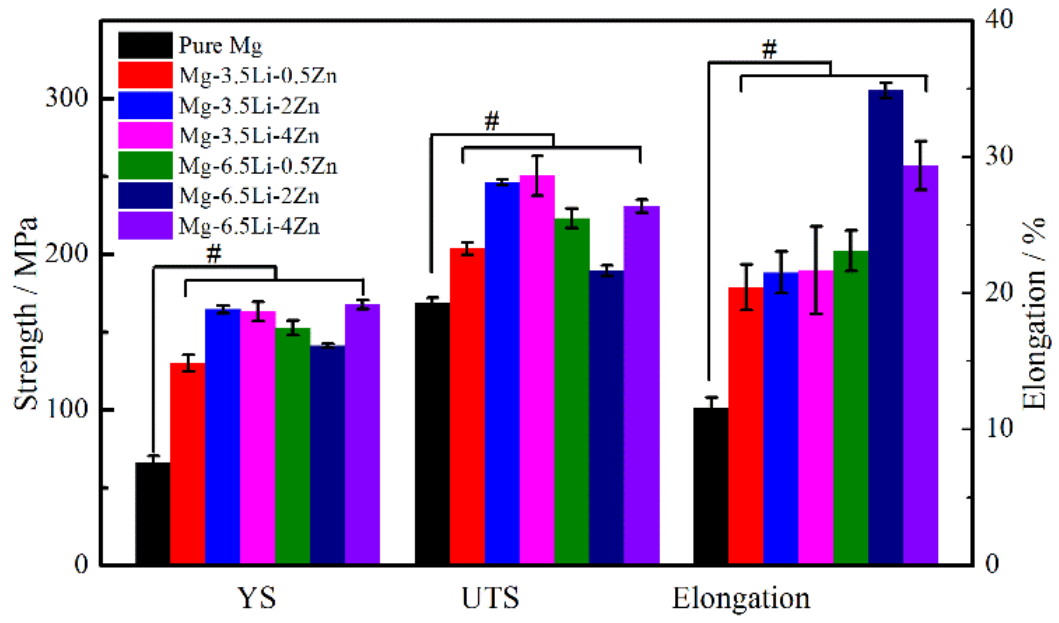
Fig.4
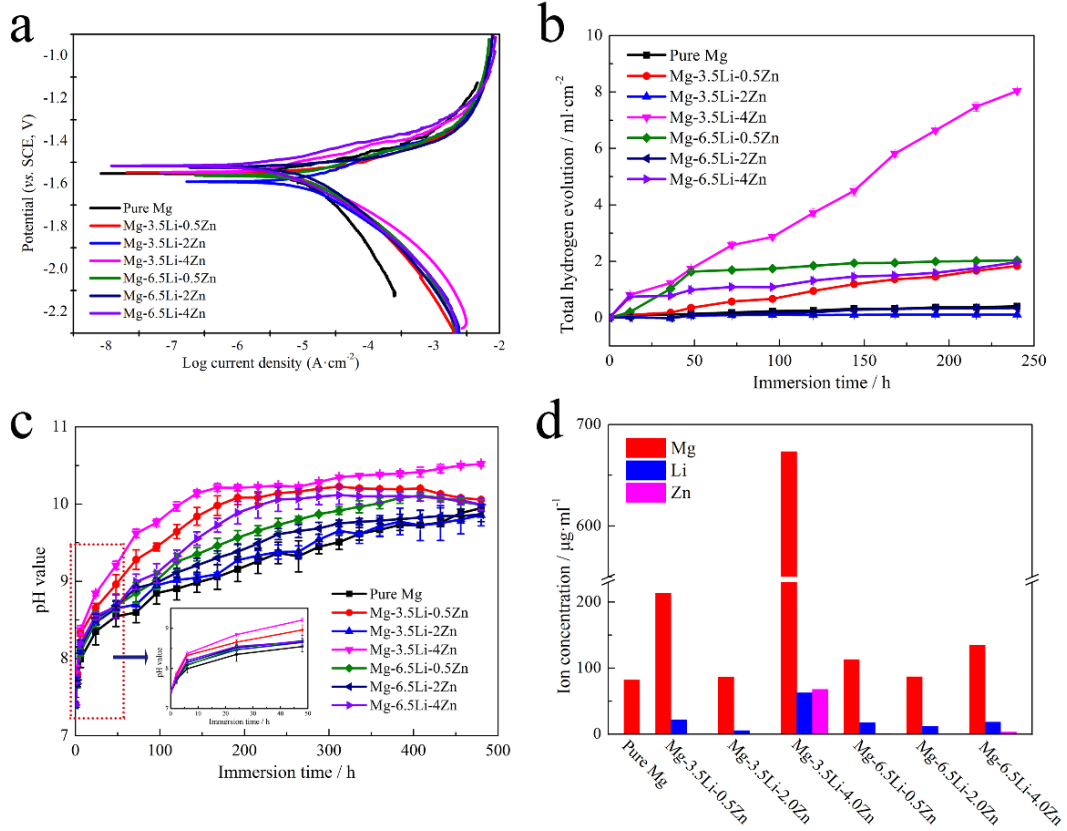
Fig.5
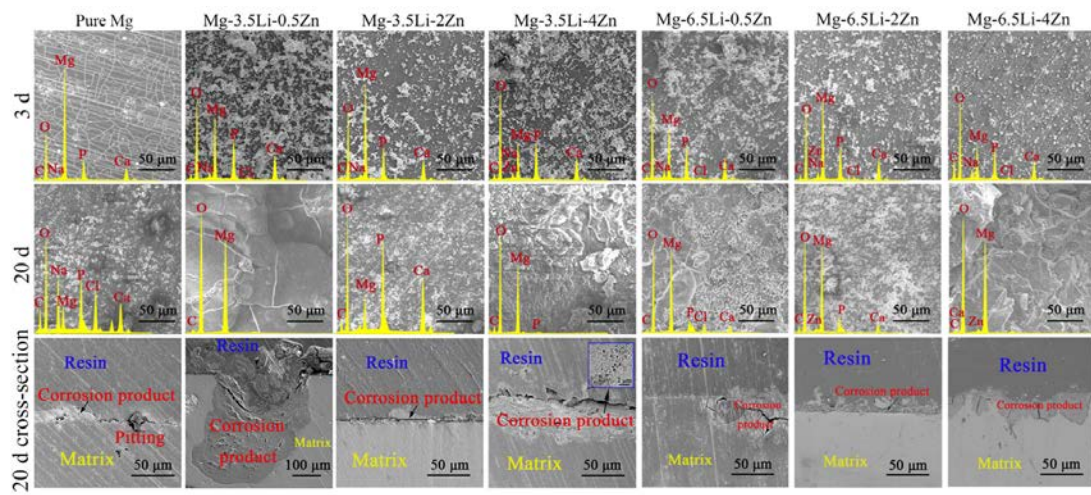
Fig.6
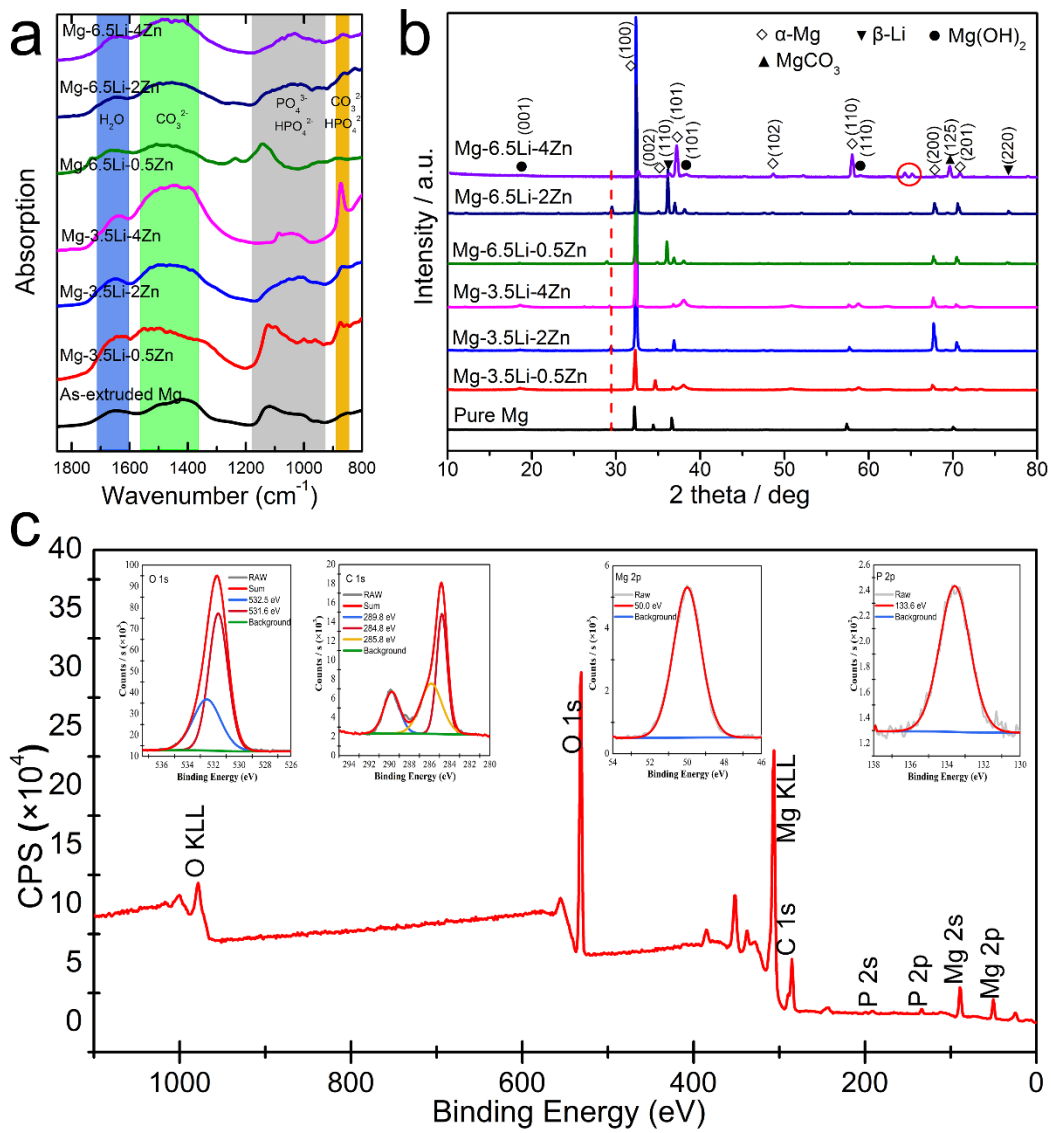
Fig.7

a VSMC
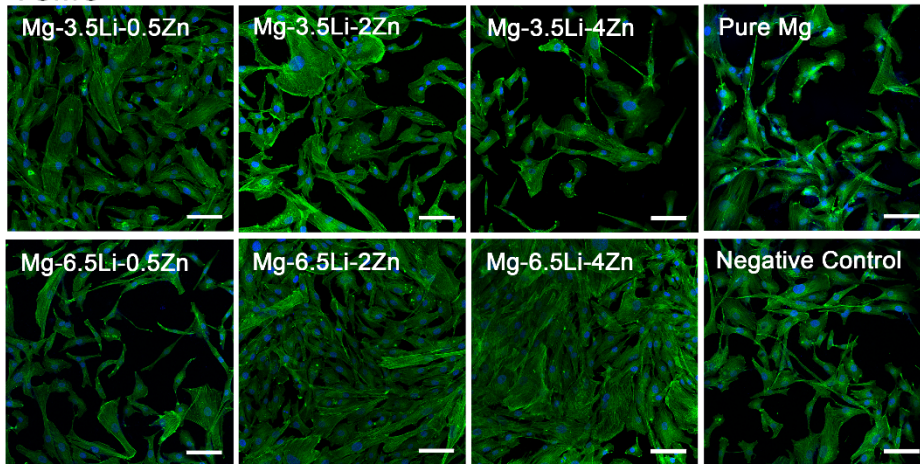
b HUVEC
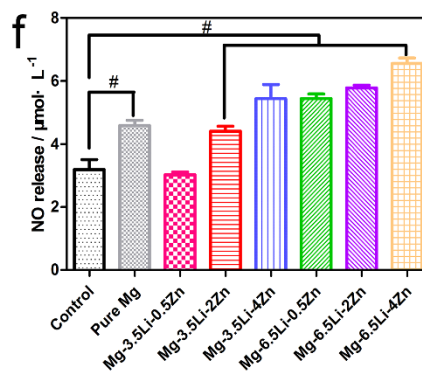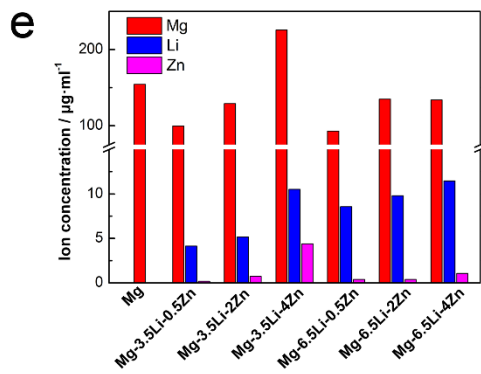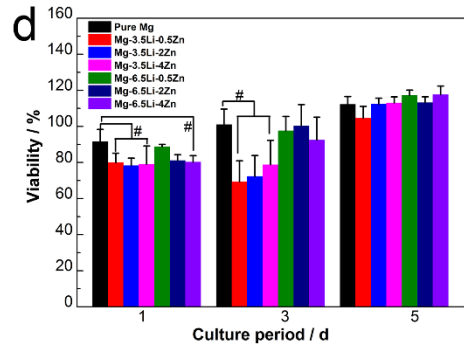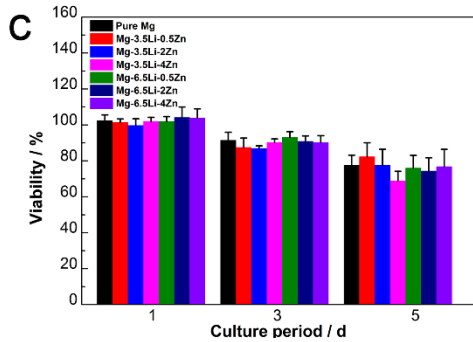
Fig.8

Fig.9

Fig.10

Fig.11

Fig.S1

Fig.S2

Fig.S3